Decomposing observations of high-frequency radar-derived surface currents by their forcing mechanisms: Decomposition techniques and spatial structures of decomposed surface currents

Sung Yong Kim,[1] Bruce D. Cornuelle,[2] and Eric J. Terrill[1]

Received 22 February 2010; revised 24 June 2010; accepted 7 July 2010; published 2 December 2010.

[1] Surface current observations from a high-frequency radar network deployed in southern San Diego are decomposed according to their driving forces: pure tides and their neighboring off-band energy, local winds, and low frequency. Several superposed ocean responses are present as a result of the complicated bottom topography and relatively weak winds off southern San Diego, as opposed to coastal regions where circulation can be explained by a dominant forcing mechanism. This necessitates an application of a statistical decomposition approach. Surface currents coherent with pure tides are calculated using harmonic analysis. Locally wind-driven surface currents are estimated by regression of observed winds on observed surface currents. The dewinded and detided surface currents are filtered by weighted least-squares fitting assuming white noise and three colored signal bands: low-frequency band (less than 0.4 cycles per day) and near-tidal peaks at the diurnal (K_1) and semidiurnal (M_2) frequencies. The spatial and temporal variability of each part of the decomposed surface currents is investigated in terms of ocean response to the driving forces. In addition, the spatial correlations of individual components exhibit Gaussian and exponential shapes with varying decorrelation length scales.

Citation: Kim, S. Y., B. D. Cornuelle, and E. J. Terrill (2010), Decomposing observations of high-frequency radar-derived surface currents by their forcing mechanisms: Decomposition techniques and spatial structures of decomposed surface currents, *J. Geophys. Res.*, *115*, C12007, doi:10.1029/2010JC006222.

1. Introduction

[2] Coastal surface current is a mixture of the oceanic responses to local winds, remote wind forcing via eddies and coastal trapped waves, tides, pressure gradients, and meteorological fluxes of heat and fresh water [e.g., *Ekman*, 1905; *Ewing*, 1950; *Munk and Cartwright*, 1966]. The components of current have distinct spatial and temporal scales reflecting distinct ocean dynamics. An appropriate partitioning of observations allows us to discern the meaningful forcing terms and responses and to deduce their interactions. Surface current maps created by shore-based high-frequency radars (HFRs) are an in situ observational resource with high density, hourly in time and km in space. They also have potential to study near-surface phenomena at submesoscale and smaller, surface circulation, and waterborne transport. In this vein, we have decomposed surface currents into their driving forces using statistical analysis and interpreted them in terms of their spatial scales and temporal variations.

[3] This paper is the first of three companion papers for surface current decomposition motivated by following questions: How much surface current variance is explained by each forcing component? What are the characteristics and variability of surface currents driven by each forcing component? How can these results be used to create a statistical surface current model based upon observations? In this paper, we focus on the techniques applied for decomposition, an overall description of current responses to potential driving forces (e.g., tides, wind, and low-frequency forces), and their spatial structure. Detailed investigations on the individual current components (e.g., locally wind-driven and tide-coherent surface currents) are addressed in the other companion papers [*Kim et al.*, 2010; S. Y. Kim et al., Decomposing observations of high-frequency radar derived surface currents by their forcing mechanisms: Surface signature of M_2 internal tides, manuscript in preparation, 2010].

[1]Marine Physical Laboratory, Scripps Institution of Oceanography, University of California, San Diego, La Jolla, California, USA.
[2]Climate, Atmospheric Science and Physical Oceanography, Scripps Institution of Oceanography, University of California, San Diego, La Jolla, California, USA.

0148-0227/10/2010JC006222

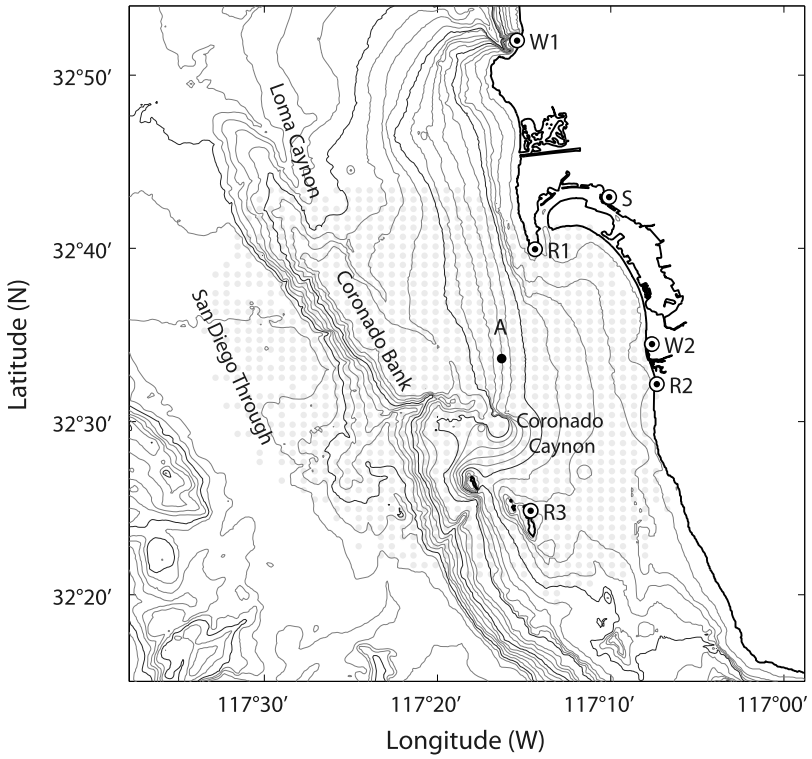

Figure 1. Study domain for decomposition of surface currents using in situ observations: surface currents from three HFRs (Point Loma (SDPL, R1), Border Park (SDBP, R2), and Coronado Islands (SDCI, R3)), coastal winds at two shore stations (Scripps Pier (SIO, W1) and Tijuana River (TJR, W2)), and surface tides at San Diego Bay (SDB, S). The gray dots indicate the grid points that have at least 70% data availability of surface currents for 2 years (April 2003 to March 2005). A decomposed surface current time series at the location A is shown as an example in Figure 4. The bottom bathymetry contours are indicated by thin curves with 10 m ($0 < z < 100$ m) and 50 m ($100 < z < 1000$ m) contour intervals and thick curves at the 50, 100, 500, and 1000 m depths.

[4] There is precedence in the literature of separating currents based upon their forcing such as decomposing tidal currents and residual currents using harmonic analysis and band-pass filters [e.g., *Prandle*, 1987; *Shay et al.*, 1995]. Moreover, the locally wind-driven surface currents were estimated from the detided surface currents in two ways: a simple regression between surface currents and winds [e.g., *Essen et al.*, 1983; *Prandle and Player*, 1993] and a fit using rotary empirical orthogonal functions (EOFs) [e.g., *Ng*, 1993]. Surface currents off southern San Diego contain mixed current responses to several driving forces and their interactions: pure tides, diurnal (plus harmonics) wind, broad-band wind, diurnal heat flux, and both cross-shore and alongshore pressure gradients. Therefore the use of a band-pass filter before the separation of both locally wind-driven currents and purely tide-coherent currents can be problematic, because locally wind-driven currents can have similar spectral content as tidal currents. Moreover, the least-squares spectral analysis as an extended version of *Pawlowicz et al.* [2002] is used for missing observations instead of conventional band-pass filters.

[5] This paper is organized as follows. First, the dominant variance of in situ observations is described (section 2). Then, the applied decomposition techniques using a statistical regression and a weighted least-squares fitting method are addressed (section 3). Last, the spatial and temporal variability of decomposed surface currents and their averaged correlation are presented (section 4).

2. Observations

[6] Surface currents observed by three HFRs (~25 MHz; Point Loma (SDPL, R1), Border Park (SDBP, R2), and Coronado Islands (SDCI, R3) in Figure 1) off southern San Diego are decomposed in terms of their driving forces. Winds observed at two shore stations (Scripps Pier (SIO, W1) and Tijuana River (TJR, W2)) are converted into wind stress using the drag coefficient described by *Large and Pond* [1981]. Although other wind observations around San Diego are available, only two shore station winds in the study domain are used, because the offshore wind at the buoy (National Data Buoy Center (NDBC) 46086 station) has weak coherence with coastal winds, less than 0.5 in the subdiurnal frequency band and at the diurnal frequency and less than 0.2 in other frequencies. Moreover, the wind data at inland stations (National Climatic Data Center (NCDC)) have relatively low sampling frequency and sensor accuracy. All observations used in this study are hourly averaged over 2 years (April 2003 to March 2005). The approaches to estimate the spectral contents of each observation are summarized in Appendix A.

2.1. Surface Currents

[7] Optimally interpolated hourly surface currents are used for the decomposition analysis (see Appendix B and *Kim et al.* [2008] for more details). Surface circulation off southern San Diego is characterized by a southeastward long-term mean, near-coast counter currents (northward), anisotropic and asymmetric wind-forced responses due to coastal boundary effects, vortical phenomena including submesoscale eddies, and surface signature of semidiurnal (M_2) internal tides. Total surface currents are exponentially decorrelated in space, and the alongshore components have approximately three time longer decorrelation length scale than cross-shore currents [*Kim et al.*, 2007, 2009a, 2009b; *Kim*, 2010].

[8] The averaged rotary power spectrum of surface currents over the grid points as shown in Figure 1 exhibits clockwise-dominant tidal peaks, variance in the low-frequency band (less than 0.4 cycles per day (cpd)), frequency bands centered on diurnal and semidiurnal tides, their harmonics, and the residual variance (Figure 2a). The increased spectral energy near the major tidal constituents are attributed to nonlinear interactions with topography over the continental break/shelf and modulation by low-frequency signals [e.g., *Munk et al.*, 1965; *Munk and Cartwright*, 1966]. However, the variance of surface currents at the inertial frequency ($1.06 \leq f_c \leq 1.08$ cpd in the study domain) is not significantly above the background variance [e.g., *Bratkovich*, 1985], which might be a result of energy dissipation in the coastal region. The weak inertial variance of surface currents in this region is not due to the limitation of data record length because the 2 year record length provides enough resolution to separate the inertial frequency (f_c) and the closest diurnal frequency (K_1). Moreover, the subsurface currents observed from ADCP (28 m depth) located within the study domain show the same tendency of weak inertial variance. In addition, the surface currents measured by the HFR network along the entire U. S. West Coast (USWC) show a significant separation of the variance between two frequencies (K_1 and f_c), so the weak inertial variance appears to be local to southern San Diego.

[9] The barotropic S_1 tidal currents on the USWC have been reported as 0.08–0.17 cm s^{-1} from TOPEX/Poseidon satellite altimetry data [*Ray and Egbert*, 2004; R. D. Ray, personal communication, 2009]. Therefore we expect that the observed S_1 surface currents of 5–6 cm s^{-1} (Figure 2a) are likely to be a result of other diurnal forcing components, especially diurnal wind and diurnal stratification change due to heat flux, rather than the S_1 tide.

[10] The source of the surface current variance at the semidiurnal frequency (S_2) can be ambiguous, because it may be driven by both diurnal wind and S_2 tide. Since the wind variance at the S_2 frequency is about 10 times less than the S_1 variance, and the gravitational S_2 tidal forcing is about seven times higher than the atmospherically forced S_2 component (air tides) [e.g., *Arbic*, 2005; *Ponte and Vinogradov*, 2007], we assume that the S_2 variance

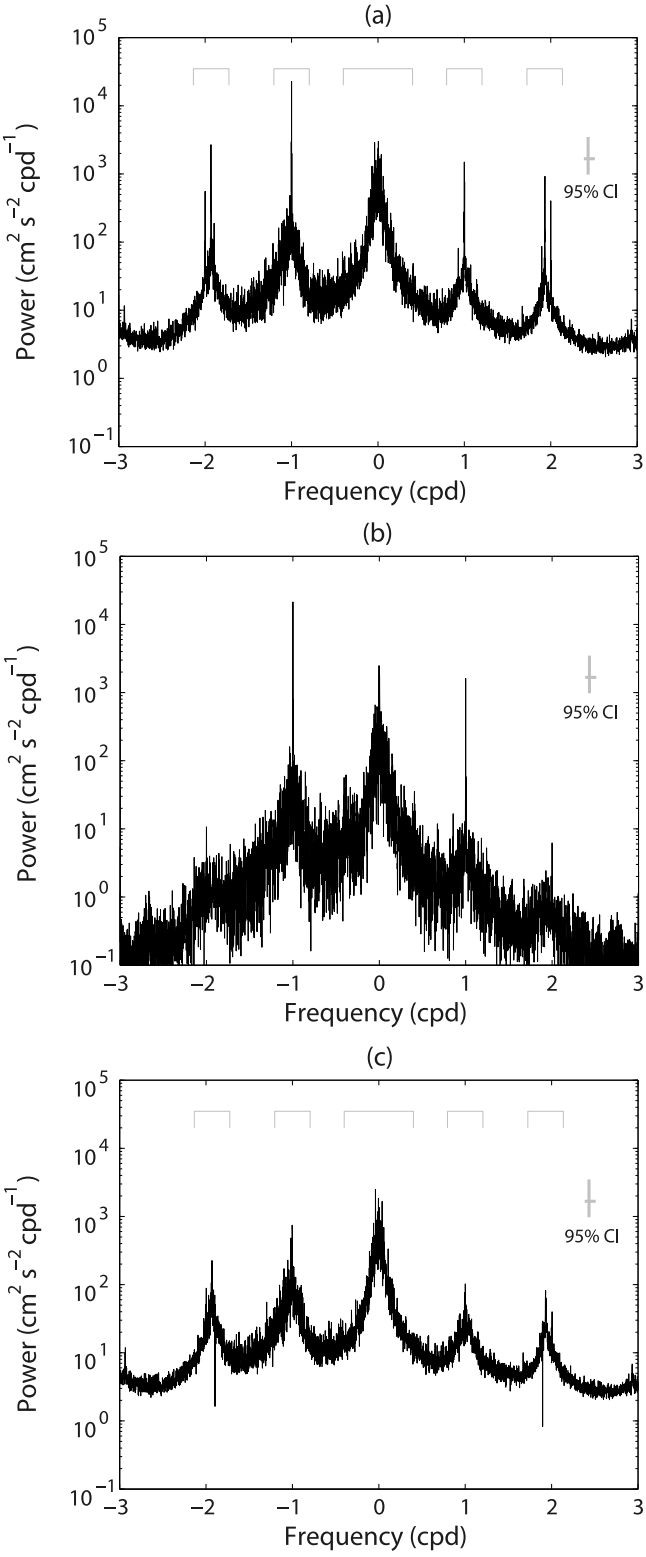

Figure 2. Regionally averaged rotary power spectra of (a) total surface currents (**u**), (b) locally wind-driven surface currents ($\mathbf{u}_W$), and (c) surface currents with both locally wind-driven and purely tide-coherent components removed ($\mathbf{u}_G$). The 95% confidence internal are indicated with a gray error bar. Three frequency bands (low-frequency and frequency bands centered at the diurnal (K_1) and semidiurnal (M_2) frequencies) are indicated on the top of Figures 2a and 2b. Negative and positive frequencies correspond to clockwise and counterclockwise rotations, respectively.

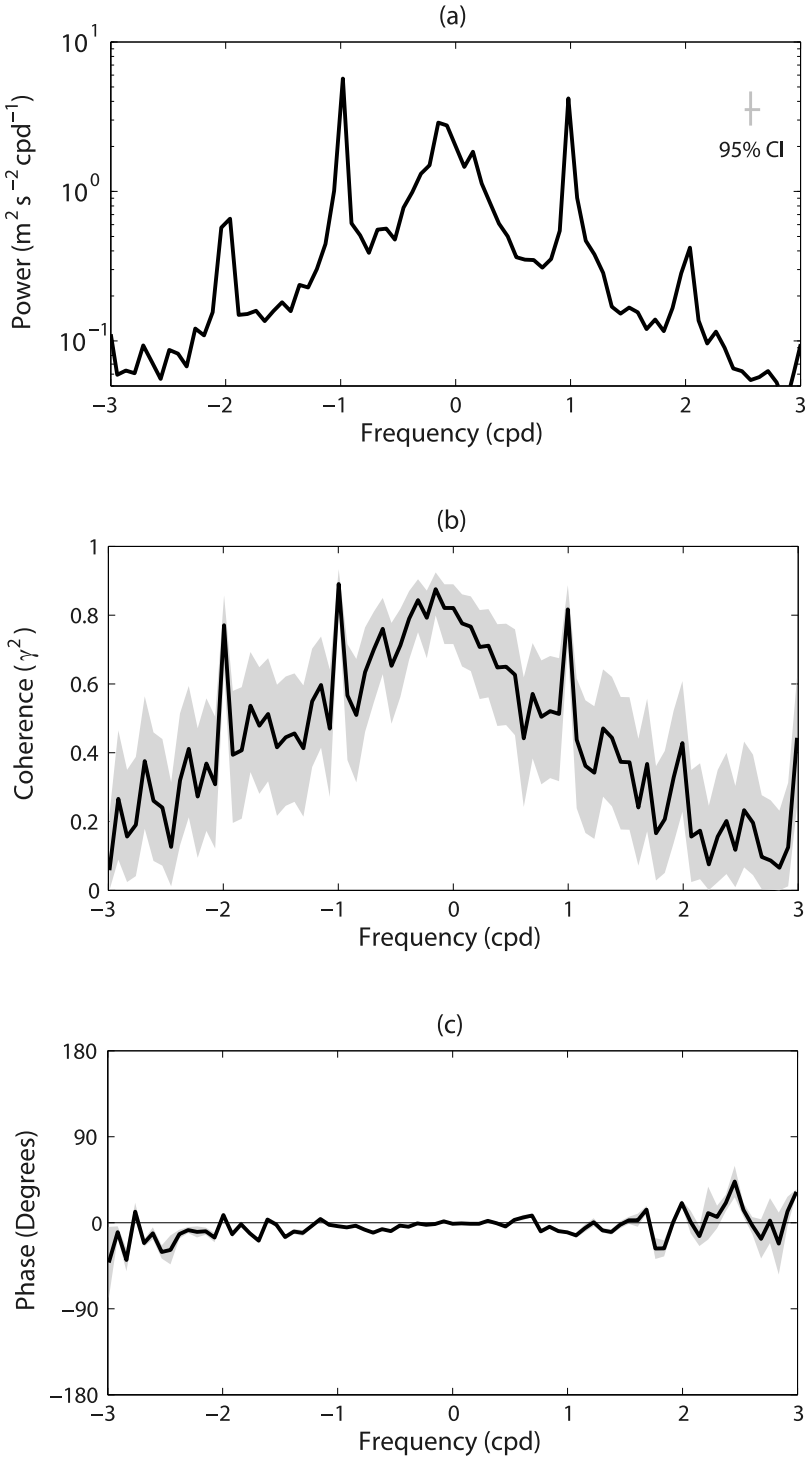

Figure 3. (a) Rotary power spectrum of the TJR wind. (b and c) Coherence and phase between SIO and TJR winds. The 95% confidence intervals are indicated as an error bar and gray shading (see Appendix A). Positive phase means the TJR wind leads the SIO wind.

of surface currents is dominantly driven by the S_2 tide [*Kim et al.*, 2009a].

2.2. Wind

[11] The rotary power spectrum of the TJR wind contains a diurnal peak and its harmonics superposed on a red spectrum (Figure 3a). Although the log-scale plot compresses the peaks, the clockwise variance at the diurnal frequency is 2–3 times greater than the counterclockwise variance at that frequency. The SIO wind spectrum (not shown) shows a similar variance distribution to the TJR wind. The rotary coherence (γ^2, see Appendix A) and phase between the two wind observations are shown in Figures 3b and 3c, respectively. Statistically significant

Table 1. Amplitudes of Surface Tides at San Diego Bay

Constituents	Constituents Name	Frequency (cpd)	Amplitude (m)	Phase (deg)
M_2	Principal lunar semidiurnal	1.9323	0.576	148.9
K_1	Lunar solar diurnal	1.0027	0.352	210.5
S_2	Principal solar semidiurnal	2.0000	0.233	145.9
O_1	Principal lunar diurnal	0.9295	0.218	195.6
N_2	Larger lunar elliptic semidiurnal	1.8960	0.136	128.7
P_1	Principal solar diurnal	0.9937	0.109	208.8
S_1	Solar diurnal	1.0000	0.000	0

coherence (0.6–0.8) is found at the diurnal (S_1) and (solar) semidiurnal (S_2) frequencies, and in the subdiurnal frequency band ($|\omega| < 1$ cpd). The phases are nearly zero in the subdiurnal frequency band and fluctuate inside larger confidence intervals in the high-frequency band ($|\omega| > 2$ cpd). The 95% confidence intervals are indicated by gray shading (see Appendix A). In the time domain, the hodograph (not shown) of the hourly composite mean of SIO and TJR winds with respect to the local time shows dominant land/sea breezes and northeast-southwest orientation in their direction. A slight difference in the orientation between both sites is presumably due to the local geography.

2.3. Surface Tides

[12] The SIO sea surface height (SSH) shows lower coherence (γ^2) with the SSHs at the other tide gauge stations on the USWC than San Diego Bay (SDB) SSH (by roughly 0.1), especially in the subinertial frequency band. Moreover, the SIO SSH anomaly (SSHA) time series have inconsistencies compared with SSHAs at nearby stations. Therefore the SDB SSH is used to estimate the pure tide component although it may be biased by inner harbor effects and less exposed to local wave setup. The power spectrum of the SDB SSH (not shown) shows that the semidiurnal variance is stronger than the diurnal variance ($M_2 > K_1 > S_2 \simeq O_1$) as shown by the SDB tidal constituents listed in Table 1.

3. Methods

[13] The (total) surface currents ($\mathbf{u}$) are decomposed according to their driving forces sequentially [e.g., *Kirwan et al.*, 1979; *Winant and Bratkovich*, 1981]

$$\begin{aligned}\mathbf{u} &= \mathbf{u}_\mathrm{T} + \mathbf{u}_\mathrm{F} \\ &= \mathbf{u}_\mathrm{T} + \mathbf{u}_\mathrm{W} + \mathbf{u}_\mathrm{G} \\ &= \mathbf{u}_\mathrm{T} + \mathbf{u}_\mathrm{W} + \mathbf{u}_{\widehat{\mathrm{L}}} + \mathbf{u}_{\widehat{\mathrm{D}}} + \mathbf{u}_{\widehat{\mathrm{S}}} + \mathbf{u}_\mathrm{R},\end{aligned} \tag{1}$$

where $\mathbf{u}_\mathrm{T}$, $\mathbf{u}_\mathrm{W}$, and $\mathbf{u}_\mathrm{G}$ denote the surface currents driven by pure tides, the locally wind-driven surface currents, and the surface currents with both wind-driven and purely tide-coherent components removed, respectively. The remaining surface currents ($\mathbf{u}_\mathrm{G}$) are the sum of low-frequency ($\mathbf{u}_{\widehat{\mathrm{L}}}$) and diurnal frequency band ($\mathbf{u}_{\widehat{\mathrm{D}}}$), which includes the inertial surface currents, semidiurnal frequency band ($\mathbf{u}_{\widehat{\mathrm{S}}}$) components, and residual surface currents ($\mathbf{u}_\mathrm{R}$).

[14] Under the assumption that the locally wind-driven surface currents and the surface currents coherent with pure tides result from independent forcing sources, although they interact, the tidal currents including the S_2 variance are filtered out first, then the locally wind-driven surface currents are separated later.

3.1. Harmonic Analysis

[15] The surface currents phased locked with tidal constituents are filtered using least-squares fitting for major tidal constituents except for the S_1 frequency (Table 1). This least-square fit includes the nodal correction, so the computed phases are nearly identical to *Pawlowicz et al.* [2002]. This approach can improve the performance because there is no extra interpolation for missing observations.

[16] The lunar nodal shift with 18.6 year periodicity is not distinguishable from other low-frequency variability given in our record length, and the lunar fortnightly and spring-neap tides with 13.661 and 14.765 day periods are not included in this fit because they do not present as peaks in the power spectrum. Moreover, fits with and without these components do not change our results.

3.2. Wind Impulse Response Function

[17] The impulse response function ($\mathbf{H}$) in the discrete time domain (Δt) is estimated from the detided surface currents ($\mathbf{u}_\mathrm{F}$) and wind stress ($\mathbf{T}$)

$$\mathbf{H}(\mathbf{x}) = \Big(\langle \mathbf{u}_\mathrm{F}(\mathbf{x},t)\mathbf{T}^\dagger(t)\rangle\Big)\Big(\langle \mathbf{T}(t)\mathbf{T}^\dagger(t)\rangle + \mathbf{R}_\mathbf{a}\Big)^{-1}, \tag{2}$$

where $\mathbf{T}(t) = [\boldsymbol{\tau}(t - N\Delta t) \cdots \boldsymbol{\tau}(t - \Delta t)\ \boldsymbol{\tau}(t)]^\dagger$ denotes the wind stress matrix stacked with up to N hour time lags. $\boldsymbol{\tau}(t)$ is a two-element vector to allow for anisotropic response [e.g., *Kim et al.*, 2009a], i.e., $\boldsymbol{\tau}(t) = [\tau_x(t)\ \tau_y(t)]^\dagger$. The covariance matrices in equation (2) are computed excluding the missing data. The regularization matrix ($\mathbf{R}_\mathbf{a}$) is assumed to be a scaled identity matrix

$$\mathbf{R}_\mathbf{a} = \alpha^2\mathbf{I}, \tag{3}$$

with α^2 adjusted to minimize the error in the cross-validated current estimates and to stabilize the possibly nonpositive definite covariance of the wind stress due to missing observations [e.g., *Inman*, 1975; *Kim et al.*, 2009a]. This variable (α^2) is also called a Lagrangian multiplier or a trade-off parameter between model constraint and data misfit. The locally wind-driven surface currents are computed as the convolution of the response function ($\mathbf{h}(n\Delta t)$) and wind stress ($\boldsymbol{\tau}(n\Delta t)$) at each time lag ($n = 0,1, \cdots, N$)

$$\mathbf{u}_\mathrm{W}(\mathbf{x},t) = \sum_{n=0}^{N} \mathbf{h}(\mathbf{x}, n\Delta t)\boldsymbol{\tau}(t - n\Delta t). \tag{4}$$

3.3. Surface Currents in Frequency Bands

[18] Significant variance and peaks at the tidal constituents (Figure 2a) and diurnal wind (Figure 2b) are excluded by the tide and wind models (sections 3.1 and 3.2). The power spectrum of remaining surface currents ($\mathbf{u}_G$) shows dominant variance in three frequency bands and an obvious drop at the N_2 frequency (Figure 2c). Since the observation time series are not complete, band-pass filtering in the three frequency bands is accomplished by weighted least-squares fitting [e.g., *Priestley*, 1981; *Wunsch*, 1996], in spite of the computational expense. The frequencies are equally spaced and cover the bands just as used in conventional Fourier analysis, but the background spectrum outside the frequency bands with enhanced energy is treated as noise. This approach allows us to handle missing observations appropriately and to avoid an arbitrary interpolation step in order to make complete time series for a specific frequency band filtering

$$\begin{aligned}\mathbf{u}_G &= \mathbf{u}_{\widehat{L}} + \mathbf{u}_{\widehat{D}} + \mathbf{u}_{\widehat{S}} + \mathbf{u}_R \\ &= \left[\mathbf{G}_{\widehat{L}}\mathbf{G}_{\widehat{D}}\mathbf{G}_{\widehat{S}}\right]\begin{bmatrix}\mathbf{m}_{\widehat{L}}\\ \mathbf{m}_{\widehat{D}}\\ \mathbf{m}_{\widehat{S}}\end{bmatrix} + \mathbf{u}_R \\ &= \mathbf{G}\mathbf{m} + \mathbf{u}_R, \end{aligned} \tag{5}$$

where $\mathbf{G}$ denotes the regression bases, which are the stacked arrays of sine and cosine functions for regression on the low, diurnal, and semidiurnal frequency bands ($\mathbf{G}_{\widehat{L}}$, $\mathbf{G}_{\widehat{D}}$, and $\mathbf{G}_{\widehat{S}}$). These frequency bands correspond to $0 < |\omega| \le 0.4$ cpd, $0.8 \le |\omega| \le 1.2$ cpd, and $1.7 \le |\omega| \le 2.2$ cpd, respectively, marked as gray brackets in Figures 2a and 2c. The model coefficients ($\mathbf{m}$) are estimated by

$$\begin{aligned}\widehat{\mathbf{m}} &= \mathbf{P}\mathbf{G}^\dagger\left(\mathbf{G}\mathbf{P}\mathbf{G}^\dagger + \mathbf{R_b}\right)^{-1}\mathbf{u}_G \\ &= \left(\mathbf{G}^\dagger\mathbf{R_b}^{-1}\mathbf{G} + \mathbf{P}^{-1}\right)^{-1}\mathbf{G}^\dagger\mathbf{R_b}^{-1}\mathbf{u}_G, \end{aligned} \tag{6}$$

where $\mathbf{P}$ and $\mathbf{R_b}$ denote the model covariance matrix and the error covariance matrix, respectively [*Wunsch*, 1996]. The second line of equation (6) is applied in this analysis because of the computational expense required for the matrix inversion, i.e, twice the number of frequencies to be estimated (1902 basis functions from 951 frequencies for sine and cosine functions) is less than the length of the time series (17544 time records).

[19] The model covariance matrix ($\mathbf{P} = \langle \mathbf{m}\mathbf{m}^\dagger \rangle$) is the prior estimate of the spectral covariance matrix. The diagonal term of the model covariance matrix is the expected variance at each frequency, and the off-diagonal terms are the cross correlation of Fourier coefficients between different frequencies. The model covariance matrix is a diagonal matrix for a stationary process and can be separated into blocks by each frequency component

$$\mathbf{P} = \begin{bmatrix}\mathbf{P}_{\widehat{L}} & \mathbf{0} & \mathbf{0}\\ \mathbf{0} & \mathbf{P}_{\widehat{D}} & \mathbf{0}\\ \mathbf{0} & \mathbf{0} & \mathbf{P}_{\widehat{S}}\end{bmatrix}, \tag{7}$$

where $\mathbf{P}_{\widehat{L}} = \langle \mathbf{m}_{\widehat{L}}\mathbf{m}_{\widehat{L}}^\dagger \rangle$, $\mathbf{P}_{\widehat{D}} = \langle \mathbf{m}_{\widehat{D}}\mathbf{m}_{\widehat{D}}^\dagger \rangle$, and $\mathbf{P}_{\widehat{S}} = \langle \mathbf{m}_{\widehat{S}}\mathbf{m}_{\widehat{S}}^\dagger \rangle$. The variance conservation between the discrete Fourier transform and the weighted least-squares fitting approach is discussed in Appendix A.

[20] The error covariance matrix ($\mathbf{R_b} = \langle \mathbf{u}_R\mathbf{u}_R^\dagger \rangle$) is estimated from the power spectrum of the residual surface currents ($\mathbf{u}_R$)

$$S(\omega) \propto \omega^{-\beta}, \tag{8}$$

which can be assumed as the power spectrum with white noise ($\beta = 0$) or Brownian/Gaussian noise ($\beta = 2$). The power spectrum of the background currents (Figure 2c) is approximately

$$S(\omega) = \frac{9}{\omega + 3}. \tag{9}$$

However, because of the conversion of the nonwhite error spectrum to a nondiagonal matrix in the time domain and the computational burden of the matrix inversion in the second line of equation (6), we assumed the power spectrum of the error covariance matrix to be white with $S(\omega) = 1$ cm^2 s^{-2} cpd^{-1}, which is the floor level (~5 cm s^{-1}, $\Delta\omega = 1/731$ days = 0.0014 cpd) in Figure 2c.

4. Results

[21] A set of time series of decomposed surface currents at location A (Figure 1) on year days 145–155 of 2003 is shown in Figure 4. In this example, the total surface currents are mainly a sum of the locally wind-driven and low-frequency components (A, C, and D in Figure 4). The local winds are typical diurnal land/sea breezes of 0.5–4 m s^{-1} speed, and their directions are eastward on year days 146–149 and become northward on year days 150–155 (W1 and W2 in Figure 4). The locally wind-driven surface currents capture a footprint of local winds and seem to be smooth, because the regularization is designed to filter out the noise in the wind data (C in Figure 4) (see *Kim et al.* [2009a] for more details). The persistent south/southeastward components in the total surface currents are from the contribution of low-frequency components (D in Figure 4). In the tide-coherent surface currents, M_2 tidal surface currents are dominantly visible and the amplitude fluctuations are due to the linear modulation between major tidal constituents (B in Figure 4). In a similar way, the surface currents in the bands near pure tides (K_1 and M_2) appear as time series modulated by low-frequency components (E and F in Figure 4). The residual surface currents are likely to contain observational errors and intermittent current components, which are not coherent with tides, wind, and low-frequency forcing (G in Figure 4).

4.1. Variance of Decomposed Surface Currents

[22] The overall variance partitions of decomposed surface currents are summarized in Table 2. The low-frequency band surface currents and locally wind-driven surface currents, each have approximately one third of the total variance. Purely tide-coherent surface currents and surface currents in the diurnal and semidiurnal frequency bands represent approximately 20% of the total variance. The residual surface currents including nonlinear interactions, small-scale

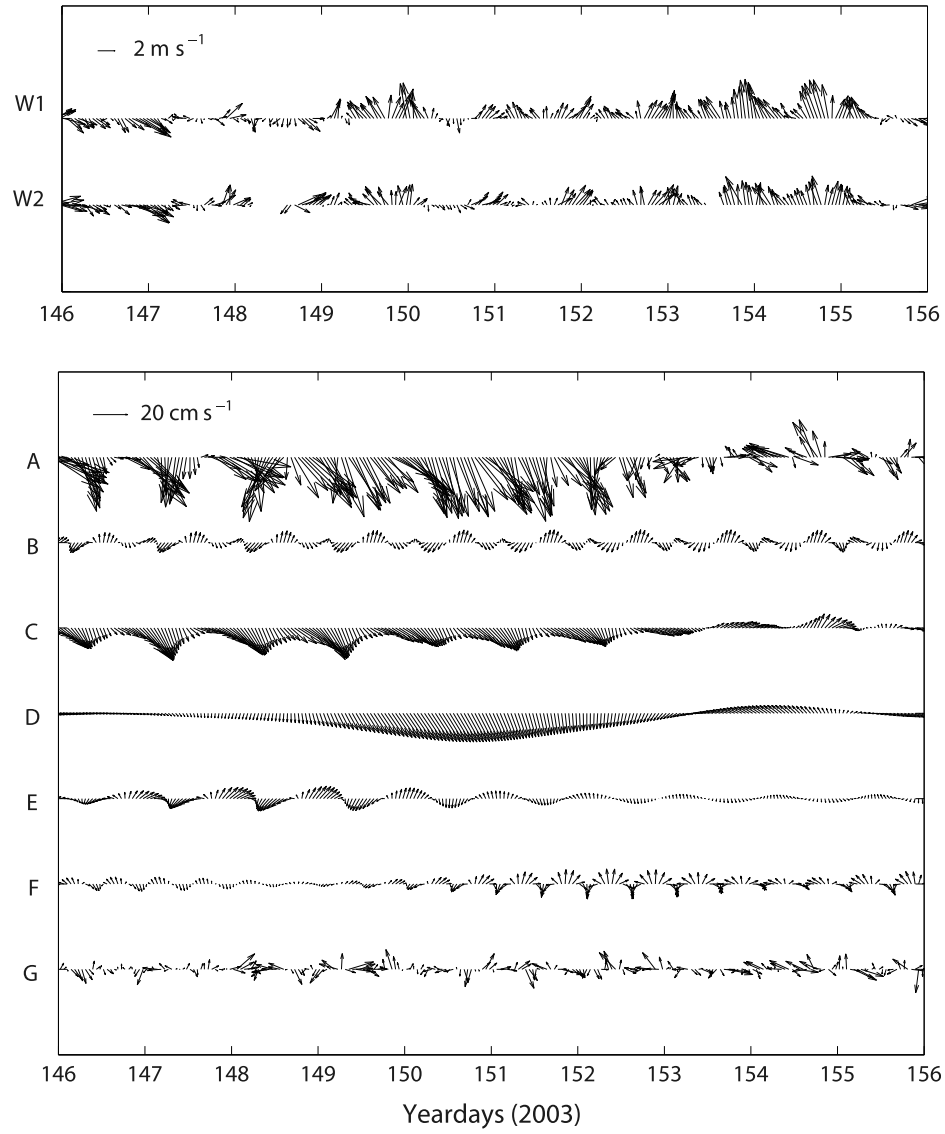

Figure 4. An example of a set of time series of local winds and decomposed surface currents at the location A in Figure 1. (top) Local winds at the SIO (W1) and TJR (W2) stations. (bottom) Total surface currents (**u**, A), surface currents coherent with pure tides ($\mathbf{u}_T$, B), locally wind-driven surface currents ($\mathbf{u}_W$, C), surface currents in the low-frequency band ($\mathbf{u}_{\widehat{L}}$, D), surface currents in the semidiurnal frequency band ($\mathbf{u}_{\widehat{D}}$, E), surface currents in the semidiurnal frequency band ($\mathbf{u}_{\widehat{S}}$, F), and residual surface currents ($\mathbf{u}_R$, G).

features, outliers, noise, observation errors account for about 15% of total variance. For detailed descriptions on individual components, their spatial and temporal variations are presented as root-mean-square (RMS, cm s^{-1}) ellipses (Figure 5) and monthly time series of their RMS computed over all grid points (Figure 6).

4.1.1. Spatial Variation

[23] As described in section 2.1, the surface circulation off southern San Diego includes several major features: southward/southeastward long-term mean surface currents across the domain, near-coast northward counter currents, and local submesoscale eddies with 5–25 km diameter. Sometimes this mean flow veers westward or southwestward. The RMS ellipses of total surface currents partly reflects the influence of coastline boundary, less variance nearshore and more offshore, and are aligned with this typical surface circulation pattern (A in Figure 5). In addition, the weak variance at the edge of the domain can be attributed to a low signal-to-noise ratio (SNR).

[24] The purely tide-coherent surface currents reflect the surface current components driven by K_1 and M_2 tides. They

Table 2. Variance Fraction (%) of the Decomposed Surface Currents

Pure Tides	Wind	Mean	Low	Diurnal	Semidiurnal	Residual
6.3	29.8	8.9	29.1	8.2	3.7	14.0

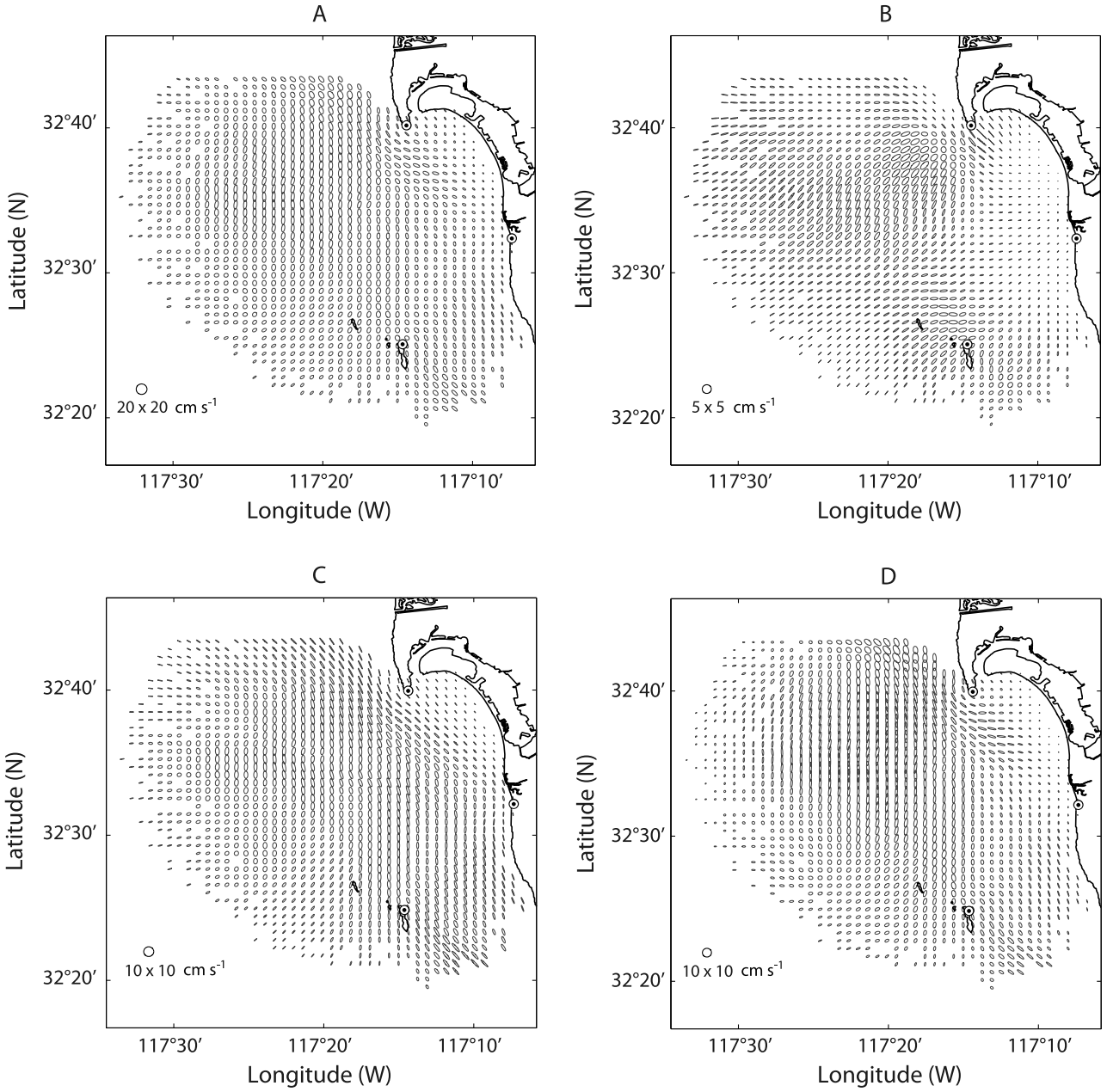

Figure 5. RMS ellipses of decomposed surface currents (cm s^{-1}). See Figure 4 for the notation of decomposed surface currents. Two artifacts at SDBP (287°T, arrow a) and SDCI (325°T, arrow b) are indicated (see G).

have high RMS in the west of Point Loma and along the Coronado Bank as shown in tidal ellipses at K_1 and M_2 frequencies (B in Figure 5 and Figure C1). Surface current observations using HFR, averaged over upper $O(1)$ m, can contain both barotropic and baroclinic tidal components, but those components can perhaps be distinguished by variations in their spatial structure. Considering the phase of tidal ellipses (Figure C1), the K_1 and M_2 tide-coherent surface currents are considered as barotropic and baroclinic components, respectively. For example, the surface currents at the M_2 frequency present a polarization front composed of clockwise and counterclockwise ellipses in the northwest and southeast areas of the domain, respectively (see Kim et al. (manuscript in preparation, 2010) for more details). This oppositely rotating surface circulation is robust in space and persistent in time with subtidal fluctuations due to background flows. This surface circulation is partly driven by mass conservation in the coastal region according to the M_2 surface tide. The phase of M_2 surface currents exhibits onshore and offshore propagation from near Coronado Bank. In this area, the bottom slope indicates shoreward-propagating M_2 internal tides, and barotropic nearshore tidal

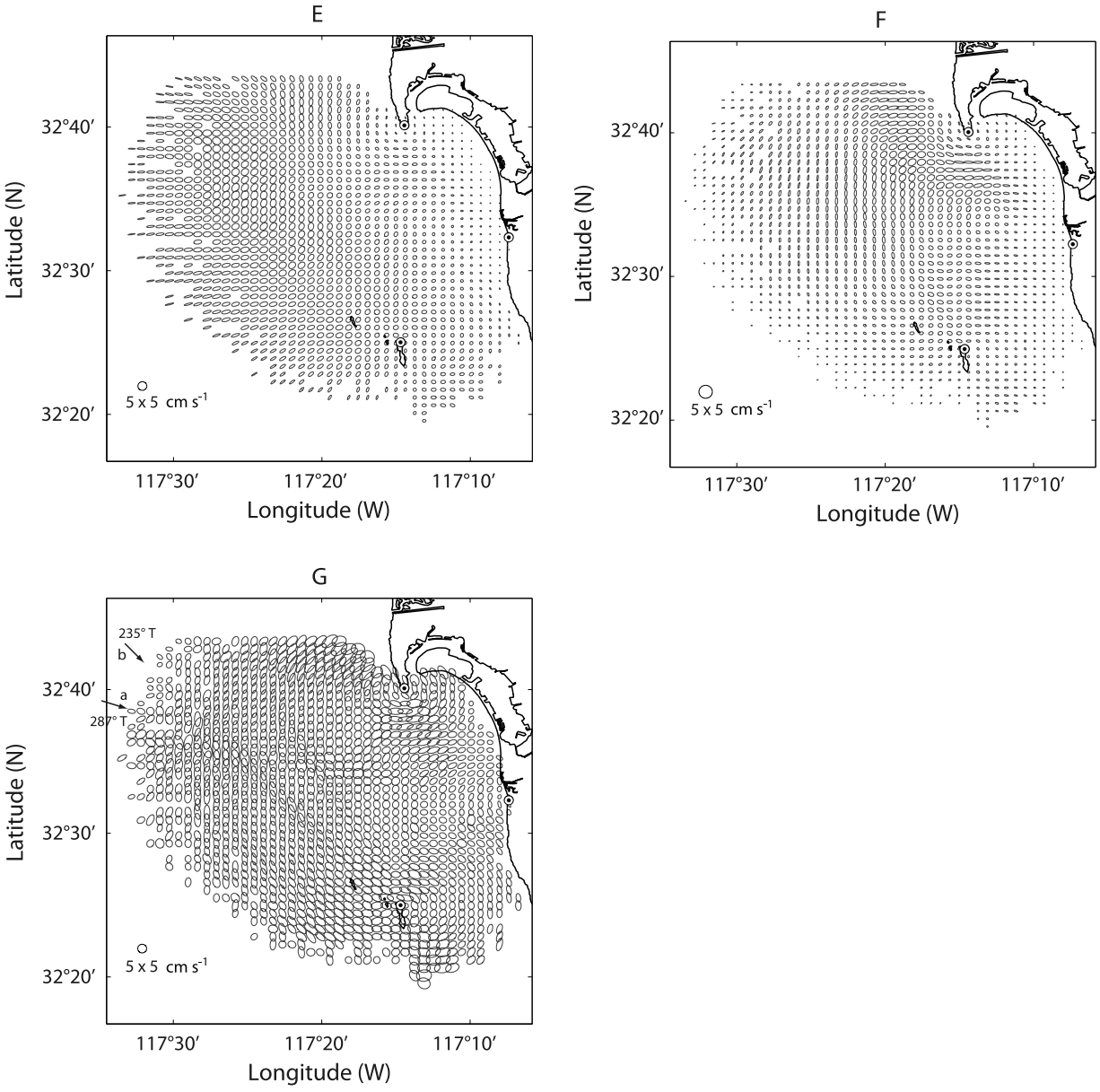

Figure 5. (continued)

models [e.g., *Spargo et al.*, 2004] expect 2–3 times stronger baroclinic M_2 currents than barotropic currents. Moreover, subsurface current and temperature profiles observed at a local mooring support the shoreward propagating M_2 internal tides. In addition, the polarized M_2 front has been reported in several coastal regions, where M_2 internal tides have been observed off Oregon [e.g., *Erofeeva et al.*, 2003], off Bodega Bay [e.g., *Kaplan et al.*, 2005], off San Francisco Bay [e.g., *Gough et al.*, 2010], Monterey Bay [e.g., *Paduan and Cook*, 1997; *Rosenfeld et al.*, 2009], and Hawaii [e.g., *Lumpkin*, 1995; *Zaron et al.*, 2009].

[25] The wind regression analysis (section 3.2) allows us to estimate the fraction of variance of surface currents explained by local winds, i.e., wind skill. The locally wind-driven surface currents at low-frequency ($|\omega| \leq 0.4$ cpd) account for over 70% of the estimated wind skill (see *Kim et al.* [2010] for more details). The wind skill map shows the skill decreasing with distance from the TJR wind station, ranging from (~0.5) nearby to (~0.25) offshore, similar to the RMS ellipses (C in Figure 5). In addition, the time mean of locally wind-driven surface currents has a spatial gradient from strong currents (7–10 cm s^{-1}) in the center of domain to relatively weak currents 1–5 cm s^{-1} offshore and nearshore (e.g., near SDB mouth). This heightened RMS distribution partly results from local geostrophic balance between sea level pressure gradients against the coast and currents [e.g., *Ponte*, 2010; *Kim et al.*, 2010].

[26] The RMS ellipses of low-frequency components more clearly show the directional preference parallel to the coast (north-south direction) than other current components (D in Figure 5). The low-frequency variability can be interpreted in the context of other in situ observations:

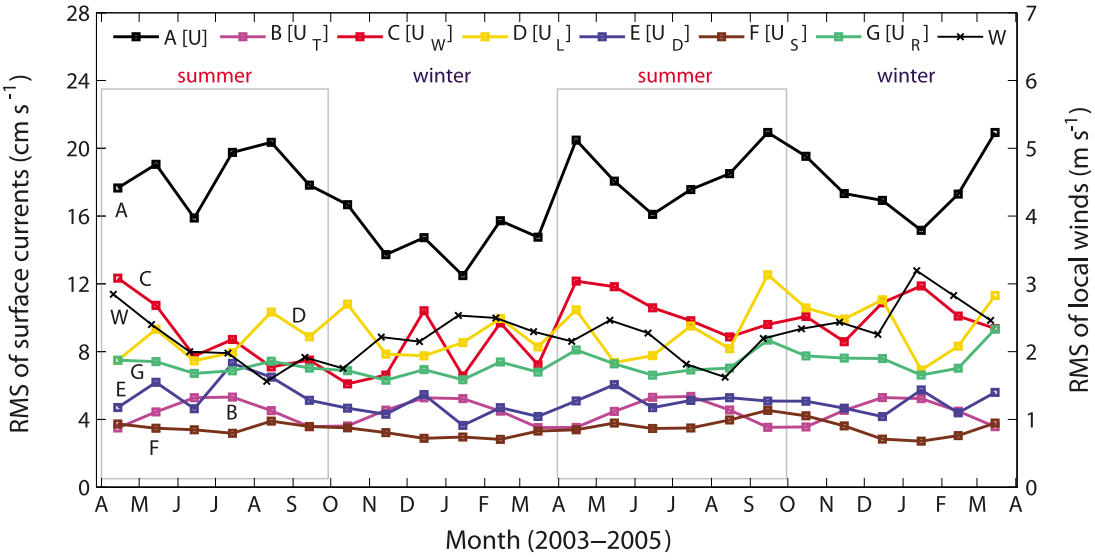

Figure 6. Temporal variation of the RMS of decomposed surface currents (cm s^{-1}) and TJR and SIO winds (W, m s^{-1}). The summer and winter indicate April–September and October–March, respectively. See Figure 4 for the notation of decomposed surface currents.

Subsurface currents at a local mooring within the study domain have oscillations with time scales of several days to weeks in the alongshore direction [e.g., *Kim*, 2010]. Moreover, alongshore surface currents off the USWC contain poleward propagating signals of about 2–3 weeks time scale. Low-frequency circulation off southern San Diego shows alternating eastward and southward surface currents approaching to Point Loma. Eastward flow slows down near the coast (Point Loma) and southward flow slides over the headland. Those flows are visible in the RMS ellipse and generate strong horizontal shear, partly related to the generation of submesoscale eddies [*Kim*, 2010].

[27] The enhanced variance of surface currents in the diurnal and semidiurnal frequency bands (Figure 2) suggests nonlinear interactions of tides with low-frequency energy. The polarization of diurnal band surface currents tends to be more clockwise as opposed to the spread polarization of semidiurnal surface currents due to mixture of clockwise and counterclockwise rotations (Kim et al., manuscript in preparation, 2010). Thus, diurnal band surface currents have more circular motion rather than elliptical motions, and their amplitudes tend to be limited by the coast (E in Figure 5 and Figure C1a). On the other hand, the semidiurnal surface currents are more elliptical and baroclinic than diurnal surface currents, similar to the spatial pattern of M_2 ellipses (F in Figure 5 and Figure C1b).

[28] The residual surface currents indicate higher RMS at the edge of the domain, behind Coronado Islands, and on baselines between radar sites (G in Figure 5). Along with those, there are artifacts in radial velocity maps due to sharp changes in the measured beam pattern of stations SDBP (287°T, arrow a) and SDCI (235°T, arrow b) (G in Figure 5) [see also *Kim et al.*, 2007; *Kim*, 2010]. The sharp change in the measured beam pattern causes an ambiguity in the bearing solution calculated from the MUSIC algorithm [e.g., *de Paolo and Terrill*, 2007]. The other one is seen along an azimuth about 325 degrees clockwise from true north of the SDCI site. The MUSIC solutions were concentrated along this radial, which led to ambiguity in the current field. This occurred at the edge of a gap in the measured beam pattern and has been investigated. These artifacts are most visible in the curl and divergence of the current field, the spatial coherence map with other in situ observations (not shown), and the residual current field (G in Figure 5). They affect less than 10% of the total grid points, so the spatially averaged covariance estimates are little changed.

4.1.2. Temporal Variation

[29] The monthly RMS time series of total surface currents (A in Figure 6) show a seasonal pattern as strong in summer (April–September) and weak in winter (October–March). This seasonality appears mainly in the surface currents in the low-frequency and diurnal frequency bands and locally wind-driven surface currents (C–E in Figure 6). Because seasonal and diurnal stratifications as well as seasonal wind forcing are dominant terms to contribute the temporal variation of the current variance.

[30] The purely tide-coherent surface currents (B in Figure 6) have semiannual beat due to K_1 and P_1 tidal constituents (Table 1). While signals of spring-neap (difference of M_2 and S_2 frequencies) and lunar fortnightly (difference of K_1 and O_1 frequencies) tides exist within this current component, they are smeared by the monthly mean.

[31] The locally wind-driven surface currents reflect the RMS of local winds (C and W in Figure 6). As local winds off southern San Diego have a seasonality with an opposite sense of total surface currents, strong in winter and weak in summer, the wind-driven surface currents are approximately out of phase with a typical seasonality in this region. Moreover, the current responses due to the diurnal wind (e.g., diurnal jets) are not visible because they are relatively less dominant compared with low-frequency variance of the wind-driven currents (see *Kim et al.* [2010] for more details).

4.2. Structure of Decomposed Surface Currents

[32] The correlation function and the approximate spatial structure of the mesoscale and submesoscale currents are presented with Gaussian or exponential functions to mirror underlying physics and variability [e.g., *Chereskin and Trunnell*, 1996; *Peters et al.*, 2002; *Paduan and Shulman*, 2004; *Kim et al.*, 2007; *Willis and Fu*, 2008]. Large-scale variability, including geostrophic and barotropic motions are expected to show more Gaussian shapes, compared to exponential shapes expected for smaller-scale processes (e.g., submesoscale and turbulence) [e.g., *Townsend*, 1980; *Denman and Freeland*, 1985; *Chereskin and Trunnell*, 1996; *Wilkin et al.*, 2002].

4.2.1. Averaged Spatial Correlation

[33] The spatially averaged correlation coefficients are presented as plan views in the spatial lag space (Δx, Δy) for each decomposed component (Figure 7, see *Kim* [2009] for three-dimensional structures). Three correlation terms of each decomposed component are shown as two diagonal terms for u components ($\overline{\rho}_{uu}$, Figure 7a) and v components ($\overline{\rho}_{vv}$, Figure 7b) and the off-diagonal term for u and v components ($\overline{\rho}_{uv}$, Figure 7c). The mean component is not considered here because it has only a single realization. The orientation of two diagonal terms ($\overline{\rho}_{uu}$ and $\overline{\rho}_{vv}$) is computed as the tilt of the major axis in a counterclockwise sense from the positive Δy axis (Table 3). Vertical sections through the correlation along this direction and the perpendicular are shown to more easily compare the correlation function of each component in the cocentered space and to quantify the decorrelation length scales in spite of their spatial complexity (Figure 8). The off-diagonal terms vary within ±0.25 with complicated shapes and do not lend themselves to simple functional descriptions (Figure 7c). However, since they are not completely zero, some dependency between u and v is likely. Note that $\overline{\rho}_{uv}$ and $\overline{\rho}_{vu}$ are not identical but mirrored in the Δx and Δy axes.

[34] The total surface currents (A in Figure 7) have the superposed structure of all decomposed components (B–G in Figure 7), which is slightly different from the spatial correlations presented previously [*Kim et al.*, 2007, Figure 12] due to the difference in the method used to extract the vector current from radial velocities: optimal interpolation now versus unweighted least-squares fitting then [*Kim et al.*, 2008]. The optimally interpolated surface currents have less noise and are smoother (see Appendix B for more details). As a result, the averaged spatial structure computed here is somewhat smoother than before, but its shape and decorrelation length scales are nearly the same. The assumed OI decorrelation scale (2 km in x and y directions) is much smaller than the scales in the spatially averaged correlation function for all decomposed surface currents, so it is not expected to influence the estimate of surface current scales. Although OI estimates are biased toward zero due to the prior assumption on the model variance and error variance, there is no significant variance reduction compared to the previous results.

[35] The purely tide-coherent surface currents have broad spatial structure in the center and complicated features near the edge of the domain (B in Figure 7) presumably owing to the large scale of the barotropic tidal forcing and the baroclinic tides having relatively smaller-scale spatial structure, respectively. In addition, the baroclinic tide-coherent surface currents have local variability when they are considered in the context of the USWC-wide barotropic tides.

[36] The locally wind-driven surface currents have the most broad spatial structure in the x and y directions of all the components (C in Figure 7), because wind-driven surface circulation in low frequency does not vary that much in the study domain. On the other hand, the limitation of available wind observations can be one reason. As winds at only two stations are used, the given analysis assumes the same winds forced surface currents on all grid points in the domain.

[37] The spatial structure of low-frequency band surface currents has clear directional orientation (D in Figure 7): u and v are highly correlated in the x and y directions, respectively, which implies the influence of the cross-shore and alongshore pressure gradients. Those pressure gradients are associated with the setups of the wind-driven sea elevation at low frequency against and along the coast, respectively [e.g., *Kim et al.*, 2010].

[38] The remaining surface current components have relatively small spatial scale variability. As described in E in Figure 5, the diurnal band surface currents have the most circular variance ellipses of all current components. This produces nearly identical correlation functions for u and v (E in Figures 7a and 7b), which have similar decorrelation length scale and orientation in both directions. The semidiurnal band surface currents have a localized structure with small ridges between 0.2 and 0.4 (F in Figure 7), which possibly are due to baroclinic tidal currents. Although the purely tide-coherent surface currents are removed, the baroclinic components still remain as enhanced variance in the tidal bands. The decorrelation length scale of the residual surface currents is the smallest of all components (G in Figure 7 and Figure 8). Since the barotropic and baroclinic currents are driven by surface pressure gradients and the tide-topographic interaction along with the stratification in the interior, respectively, they differ in the characteristics of the spatial scale as shown (B and F in Figure 7).

4.2.2. Decorrelation Length Scales

[39] The spatial correlation functions of individual surface current components are relevant to the development of mapping or assimilation technique for numerical ocean models, which often assume Gaussian correlation functions for lack of information. The correlation function estimated here appear to be Gaussian, exponential structures, or combination of the two, with different decorrelation length scales depending on underlying physics (section 4.1.1). The correlation functions of purely tide-coherent surface currents and locally wind-driven surface currents appear to be more Gaussian than exponential (B and C in Figure 7). The other correlation functions are likely to be more exponential in shape, or perhaps large-scale Gaussian with a small-scale exponential superposed (D–F in Figure 7). The one-dimensional correlation functions in the major and minor axes show these shapes more clearly (Figure 8). Since the correlation functions have the superposed shapes, using function fits to estimate the decorrelation scales may not work as well as for the total currents, which appeared more purely exponential [*Kim et al.*, 2007]. The decorrelation length scales of decomposed surface currents can be ordered

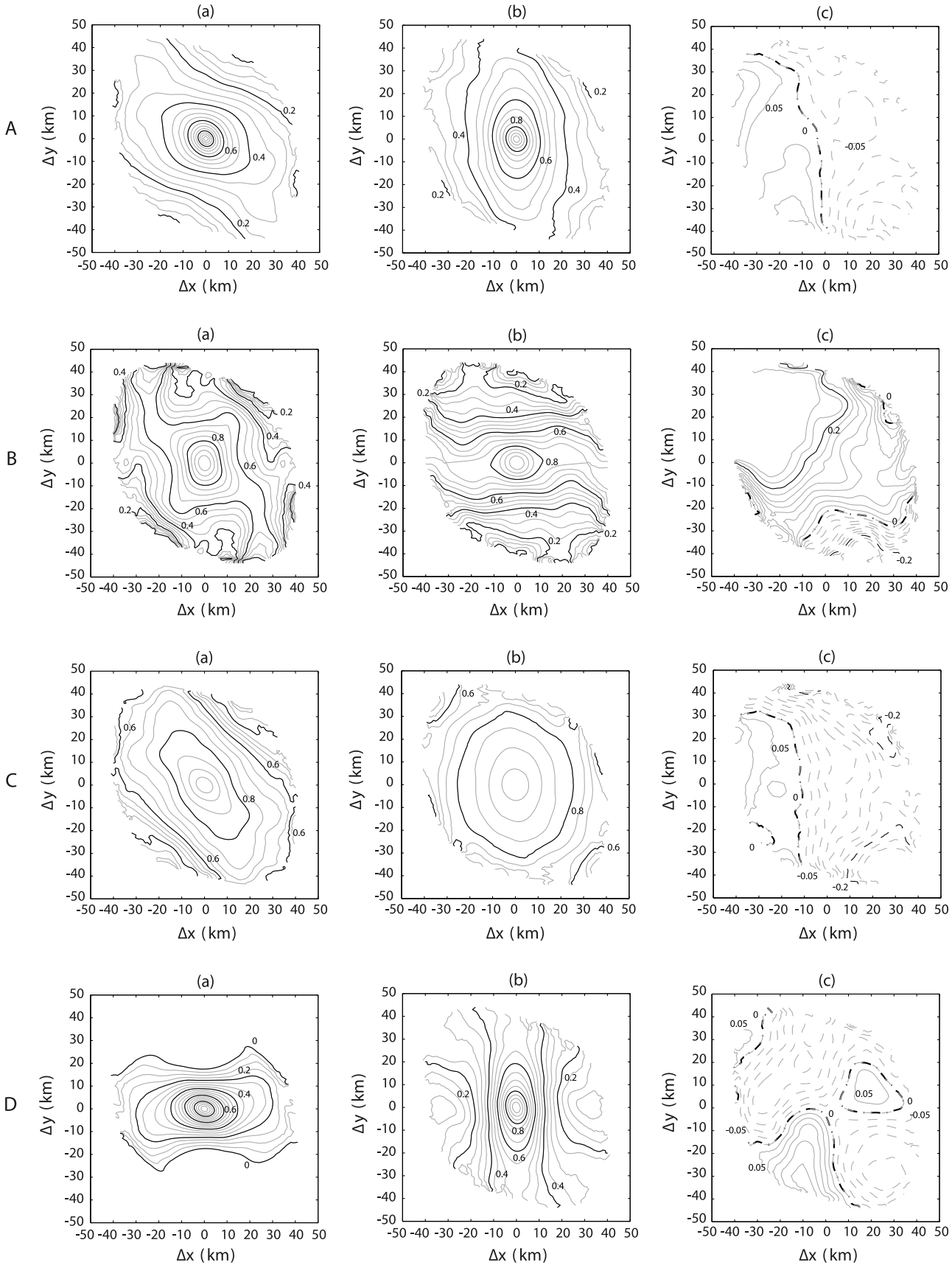

Figure 7

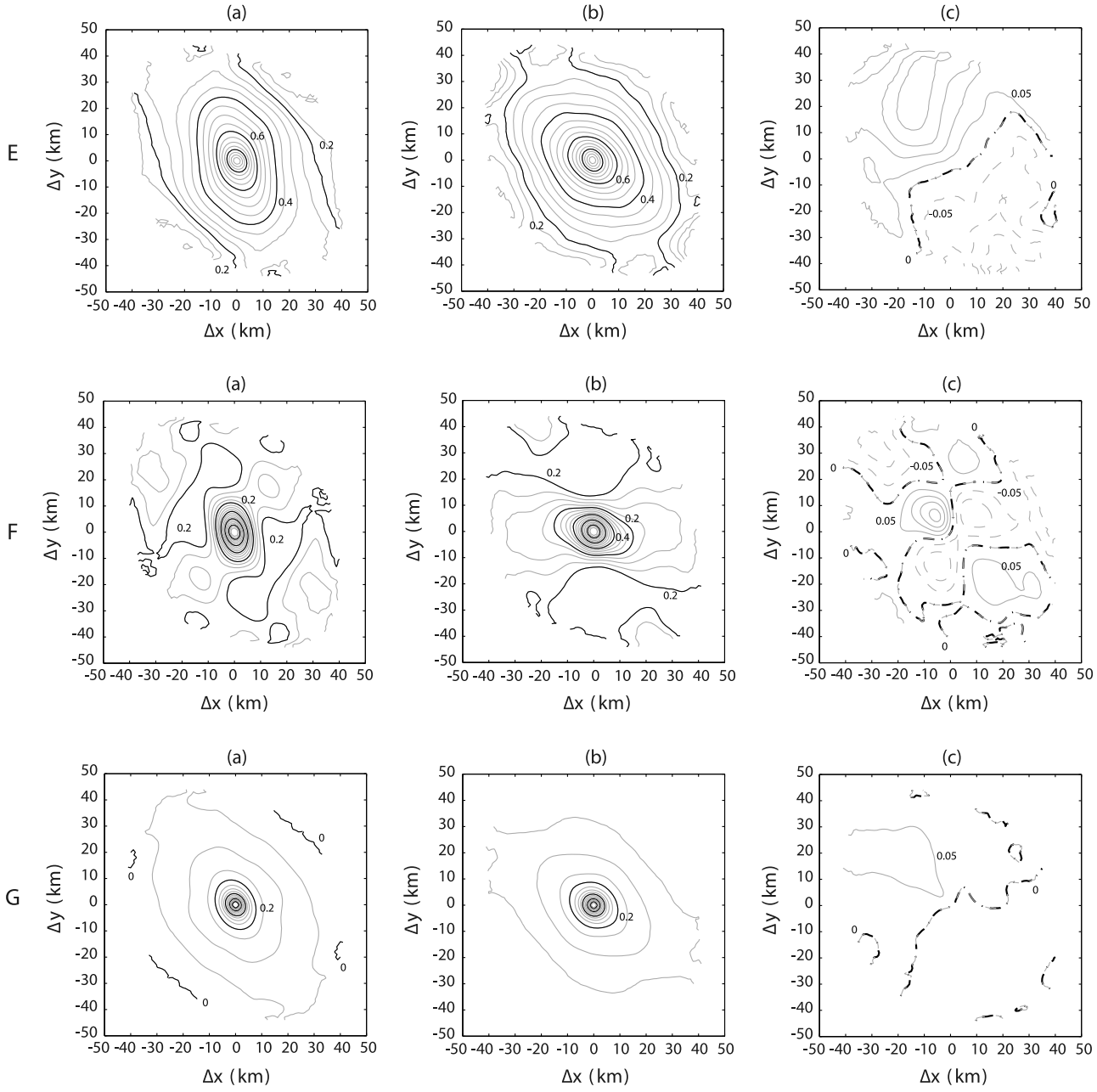

Figure 7. (continued)

in terms of the correlation in the major axis for u (Figures 8a and 8b) as

$$\lambda_W > \lambda_T > \lambda_{\widehat{D}} \approx \lambda > \lambda_{\widehat{L}} > \lambda_{\widehat{S}} > \lambda_R \tag{10}$$

and v (Figures 8c and 8d) as

$$\lambda_W > \lambda_T > \lambda_{\widehat{L}} \approx \lambda > \lambda_{\widehat{D}} > \lambda_{\widehat{S}} > \lambda_R, \tag{11}$$

where the subscript in $\lambda_{\{\cdot\}}$ indicates each component.

[40] The length scale of total surface currents (λ) is approximately the median value, consistent with the average of the length scale of individual surface current components. The switch between $\lambda_{\widehat{L}}$ and $\lambda_{\widehat{D}}$ for u and v components, respectively, may imply the dominance of alongshore and cross-shore current variability. The order of length scales in the major axis is consistent for u and v

Figure 7. Spatially averaged correlations of decomposed surface currents are presented as plan views of three components: (a) u components ($\overline{\rho}_{uu}$), (b) v components ($\overline{\rho}_{vv}$), and (c) u and v components ($\overline{\rho}_{uv}$). In the diagonal terms ($\overline{\rho}_{uu}$ and $\overline{\rho}_{vv}$), thick black contours present at 0.2, 0.4, 0.6, and 0.8 with 0.05 spacing with the gray contour. In the off-diagonal term ($\overline{\rho}_{uv}$), the dashed, solid, and dash-dotted contours indicate the negative, positive, and zero correlations, respectively. See Figure 4 for the notation of decomposed surface currents.

Table 3. Potation Angle (deg) of the Spatially Averaged Correlations of Decomposed Surface Currents is Calculated as the Tilt of the Major Axis in a Counterclockwise Sense From the Positive Δy Axis[a]

	Total	Pure Tides	Wind	Low	Diurnal	Semidiurnal	Residual
$\overline{\rho}_{uu}$	48.2	26.5	31.7	80.0	14.7	13.9	22.6
$\overline{\rho}_{vv}$	2.5	85.2	5.2	2.2	51.0	64.2	50.0

[a]See Figure 7.

(Figures 8a and 8c) unlike those for the minor axis (Figures 8b and 8d).

5. Discussion and Conclusion

[41] Surface currents measured by shore-based high-frequency radars (HFRs) are decomposed into several current components according to their driving forces and interactions of current responses: pure tides, local winds, cuspate tidal bands centered at the diurnal (K_1) and semidiurnal (M_2) frequencies, the low-frequency band (less than 0.4 cpd), and residual components. Harmonic analysis for tides, wind regression, and weighted least-squares fit for three colored signals are designed to make use of knowledge of both physical forcing mechanisms and statistics of in situ observations and to treat missing data appropriately. As an extend of this analysis, the given decomposition technique by physical driving forces is also applicable to radial velocities measured by the individual radar.

[42] The purely tide-coherent surface currents contain barotropic and baroclinic components. Their magnitude and phase allow us to distinguish two components. The M_2 tidal ellipses show the phase propagation onshore and offshore and elevated RMS over continental shelf break region, consistent with M_2 internal tides reported in other in situ observations. This suggests that the HFR be used as a potential tool to identify the surface features modulated by internal tides or baroclinic motions in coastal regions.

[43] The locally wind-driven surface currents are computed from the impulse response function between shore station winds and detided surface currents allowing for

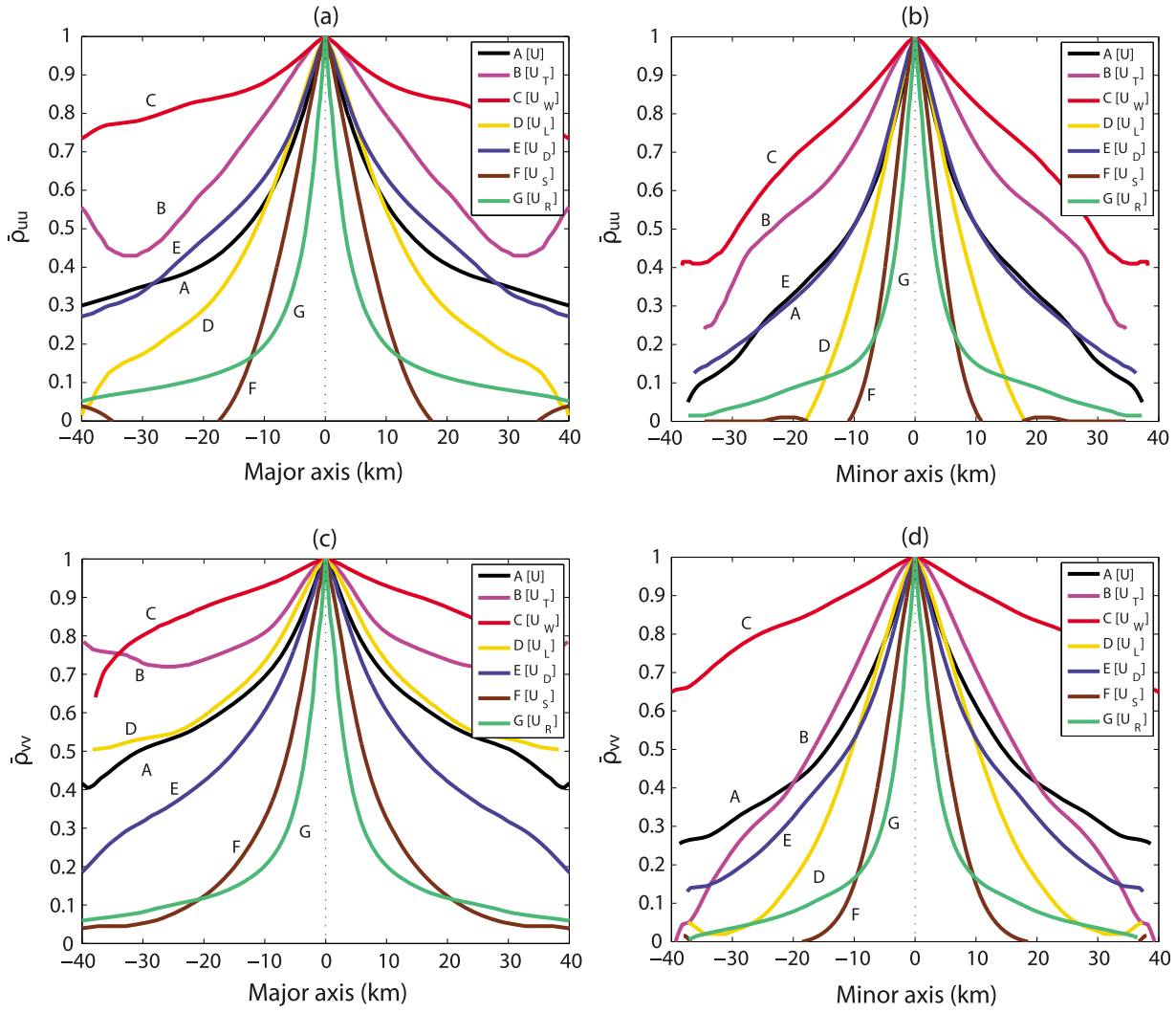

Figure 8. Spatially averaged correlations of decomposed surface currents at the (a and c) major axis and (b and d) minor axis: $\overline{\rho}_{uu}$ (Figures 8a and 8b) and $\overline{\rho}_{vv}$ (Figures 8c and 8d). See Figure 4 for the notation of decomposed surface currents.

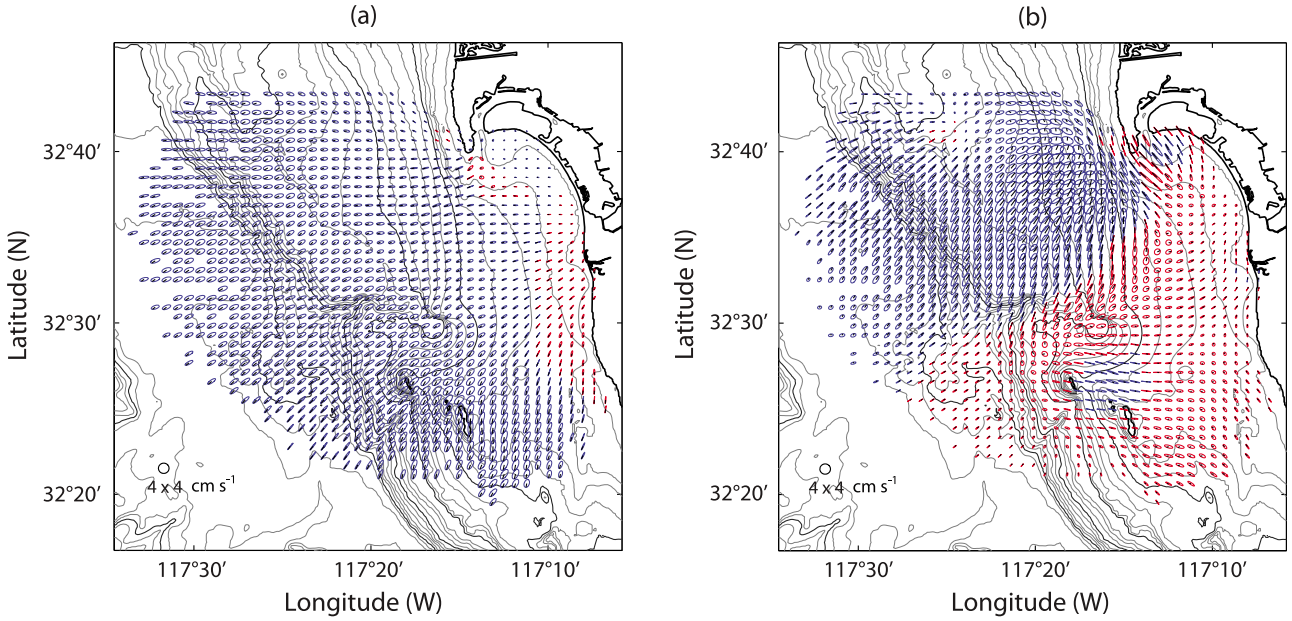

Figure C1. Tidal ellipses of surface currents estimated using the harmonic analysis at (a) K_1 and (b) M_2 frequencies. The blue and red ellipses represent clockwise and counterclockwise rotations, respectively. The black line within an ellipse indicates the phase. The units of the major and minor axes are cm s^{-1}.

anisotropic response. The approach using transfer function and response function quantifies the statistical relationship between wind and surface currents and relates to dynamics of wind-driven surface circulation. For example, the local pressure set up against the coast due to local winds is balanced with currents as local geostrophic balance, presented as increased amplitude of transfer function [e.g., *Kim et al.*, 2010]. A seasonality imposed on surface currents is not explicitly partitioned as a forcing term, however, the seasonal wind transfer function and local CTD cast data show seasonality [e.g., *Kim et al.*, 2010].

[44] The decomposed surface currents show distinct spatial structure and decorrelation length scales. The spatially averaged correlations exhibit both Gaussian and exponential shapes depending on the source of the variability and the geophysical influence, especially coastline and bottom bathymetry. The orientation of correlation function also reflects these influences.

[45] The results of decomposing the surface currents can serve as building blocks for a statistical model of the surface currents for gap filling and forecasting. Near-future currents coherent with pure tides can be computed from the estimated Fourier coefficients, and the locally wind-driven currents may have some predictability from the (anisotropic) response function driven by atmospheric forecasts. The surface current components in the three frequency bands have predictability according to their decorrelation times, but a dynamical model may be needed to optimize forecasts, for instance, low-frequency currents could be estimated from forecasts of large-scale wind and atmospheric pressure.

Appendix A: Notes on Spectral Analysis

A1. Estimates of Spectral Contents

[46] Spectral analysis, such as rotary power spectra and coherence, can help to identify dominant modes of variability in the observations and relationships between driving forces and surface current response. The power spectrum can be calculated from either the Fourier transform of the time lag covariance (Wiener-Khinchin theorem) or squared coefficients of the windowed Fourier transform of the time series [e.g., *Priestley*, 1981; *Cohen*, 1992, 1998; *von Storch and Zwiers*, 1999]. Both approaches are comparable and produce similar estimates of the dominant bands of variance in the data. Typically the Fourier transform of the time series requires complete data which is sometimes made using interpolation methods such as objective analysis to fill in the missing data. In this paper, the missing points in the time series are filled by zeros before the transform and taper functions are not used. In our data set, the fraction of missing points is generally small (less than 8%) and experiments show that zero filling slightly increases the noise level at the highest frequencies, but the identification of the dominant variability is robust. Least-squares harmonic analysis (as opposed to power spectrum estimation) was used in the band-pass filtering (section 3.3) of the time series with missing data instead of filling zeros in order to avoid contamination of the high-frequency band. For the power spectra, taper (window) functions were tested to see whether the spreading due to sidelobes affected the final spectral estimate, but no significant change in the power spectrum was observed. For example, the cuspate peaks near the diurnal and semidiurnal tides and wind are not affected by sidelobe spreading.

[47] The number of degrees of freedom (DOF, $2N$) in the spectral analysis is determined by a trade-off between the frequency resolution and confidence level of estimates. In other words, as the DOF increases, the frequency resolution of the estimates coarsens while the error bars decrease. A single time series is broken into N nonoverlapped time series with identical record lengths, and the spectral analyses for

the individual segments are averaged. For the single wind time series, N is chosen to be 50 to resolve the diurnal peak and its harmonics of the wind (section 2.2 and Figure 3).

[48] The number of spatial DOF for surface current time series at 1337 grid points used in this study is calculated as three based on the moment matching method (Figures 1 and 2). Estimates of the DOF of spatially correlated time series have been discussed [e.g., *Bretherton et al.*, 1999].

[49] The coherence (γ^2) reported in this study is referred as to

$$\gamma^2(\omega) = \frac{1}{N}\sum_{n=1}^{N}\left(\frac{|s_{12}(\omega)|^2}{s_{11}(\omega)s_{22}(\omega)}\right)_n, \tag{A1}$$

where $s_{11}(\omega)$ and $s_{22}(\omega)$ are the cospectrum of each subsampled datum, and $s_{12}(\omega)$ is the cross spectrum of them. The confidence intervals of the coherence, phase, and power spectrum are considered [e.g., *Priestley*, 1981; *von Storch and Zwiers*, 1999].

A2. Variance Conservation in the Extended Spectral Analysis

[50] A time series (**d**) can be regressed using the explicit basis of the sine and cosine functions (**G**) on the discrete frequency domain

$$\mathbf{d} = \mathbf{G}\mathbf{m}, \tag{A2}$$

$$\begin{aligned} d(t) &= a_0 + \sum_{n=1}^{N} a_n \cos\omega_n t + b_n \sin\omega_n t \\ &= a_0 + \frac{1}{2}\sum_{n=1}^{N}(a_n - ib_n)e^{i\omega_n t} + (a_n + ib_n)e^{-i\omega_n t}, \end{aligned} \tag{A3}$$

where a_n and b_n are the model coefficients (a_n and $b_n \in \mathcal{R}$). $\mathbf{m} = [a_1 \cdots a_n\ b_1 \cdots b_n]^{\dagger}$. On the other hand, the discrete Fourier transform can decompose the time series (**d**) into

$$\mathbf{d} = \mathbf{G}\hat{\mathbf{m}}, \tag{A4}$$

$$\begin{aligned} d(t) &= \sum_{m=-N}^{N} \hat{d}_m e^{i\omega_m t} \\ &= \sum_{m=-N}^{N}\left(\hat{a}_m + i\hat{b}_m\right)e^{i\omega_m t}, \end{aligned} \tag{A5}$$

where $\hat{a}_m$ and $\hat{b}_m$ are Fourier coefficients ($\hat{a}_m$ and $\hat{b}_m \in \mathcal{R}$, $\hat{d}_m \in \mathcal{C}$, $m \neq 0$). The variance conservation of two approaches in the frequency domain is

$$\langle \mathbf{d}(t)^2 \rangle = \frac{1}{2}\mathrm{trace}\left(\langle \mathbf{m}\mathbf{m}^{\dagger} \rangle\right) = \mathrm{trace}\left(\langle \hat{\mathbf{m}}\hat{\mathbf{m}}^{\dagger} \rangle\right), \tag{A6}$$

where † denotes the (complex conjugate) transpose.

A3. Relationship of Slow Least-Squares Fitting and Discrete Fourier Transform

[51] The slow least-squares fitting is converted the regular expression of the spectral analysis [e.g., *Gonella*, 1972; *Mooers*, 1973]. The data (**d**) is represented with

$$\mathbf{d}(t) = u(t) + iv(t) = \frac{1}{2}\sum_{n=1}^{N}\alpha_n e^{i\omega_n t} + \beta_n e^{-i\omega_n t}, \tag{A7}$$

where α_n and β_n are the coefficients in counterclockwise and clockwise rotations, respectively

$$\alpha_n = (a_n + d_n) + i(-b_n + c_n), \tag{A8}$$

$$\beta_n = (a_n - d_n) + i(b_n + c_n), \tag{A9}$$

$$\begin{aligned} u(t) &= \sum_{n=1}^{N} a_n \cos\omega_n t + b_n \sin\omega_n t \\ &= \frac{1}{2}\sum_{n=1}^{N}(a_n - ib_n)e^{i\omega_n t} + (a_n + ib_n)e^{-i\omega_n t}, \end{aligned} \tag{A10}$$

and

$$\begin{aligned} v(t) &= \sum_{n=1}^{N} c_n \cos\omega_n t + d_n \sin\omega_n t \\ &= \frac{1}{2}\sum_{n=1}^{N}(c_n - id_n)e^{i\omega_n t} + (c_n + id_n)e^{-i\omega_n t}. \end{aligned} \tag{A11}$$

Appendix B: Optimally Interpolated Surface Currents

[52] The surface currents are optimally interpolated from radial velocities using an isotropic exponential correlation function with a decorrelation length scale of 2 km in both x and y directions ($\lambda_0 = 2$ km). The normalized uncertainty (χ) defined as the ratio of the uncertainty variance of the estimate to the current variance is used to indicate how certain ($\chi \to 0$) or uncertain ($\chi \to 1$) the estimate is. In this study, the threshold of the normalized uncertainty is set to 0.95 in order to exclude estimates with high uncertainty both near the edge of the study domain and baselines, which are about 8% of the total data. Although the chosen threshold (χ = 0.95) is higher than used elsewhere in the literature, the uncertainty estimate is high because of the short exponential covariance used in the map, which does not reflect an optimal estimate using observed covariances. In any case, it was sufficient to exclude meaningless estimates, and the analysis and results were not sensitive to this choice. Since OI is a spatial smoothing filter, the smoothness of the current map depends on the correlation function and its decorrelation length scale. If a large-scale correlation function was used to map the data, the resulting fields would be smooth, and small-scale features would be lost. The chosen decorrelation length scale ($\lambda_0 = 2$ km) in this study allows us to preserve most variability and dynamic features, while

avoiding spurious estimates, and lowers the noise level compared with estimates using an unweighted least-squares fit. More discussion of the OI technique as used here is addressed by *Kim et al.* [2008].

Appendix C: Tidal Ellipses

[53] The purely tide-coherent surface currents are presented as tidal ellipses at K_1 and M_2 frequencies in Figures C1a and C1b, respectively.

[54] **Acknowledgments.** Sung Yong Kim is supported by the Coastal Ocean Currents Monitoring Program (COCMP) from the State of California and the Office of Naval Research (ONR). Bruce Cornuelle is sponsored by both NOAA (NOAA award NA17RJ1231) and COCMP. Eric Terrill is supported through funding provided by the ONR, COCMP, and NOAA. Surface current data are provided from the Southern California Coastal Ocean Observing System (SCCOOS, available online at http://www.sccoos.org) at Scripps Institution of Oceanography (SIO). Wind data at the Tijuana River (Tidal Linkage) are maintained by the System-Wide Monitoring Program at the Tijuana River National Estuarine Research Reserve, Estuarine Reserves Division (TRNERR), NOAA, Centralized Data Management Office (CDMO), Baruch Marine Field Lab, and University of South Carolina. Wind data at the Scripps Pier are maintained by the Integrative Oceanography Division (IOD) at SIO. The sea surface height records and harmonic constituents are provided by the Center for Operational Oceanographic Products and Services (CO-OPS) in NOAA. We thank M. Otero, L. Hazard, P. Reuter, J. Bowen, and T. Cook at Coastal Observing Research and Development Center (CORDC, available online at http://cordc.ucsd.edu) at SIO and M. Ide, M. Cordrey, and J. Crook in TRNERR.

References

Arbic, B. K. (2005), Atmospheric forcing of the oceanic semidiurnal tide, *Geophys. Res. Lett.*, *32*, L02610, doi:10.1029/2004GL021668.

Bratkovich, A. (1985), Aspects of the tidal variability observed on the southern California continental shelf, *J. Phys. Oceanogr.*, *15*, 225–239.

Bretherton, C. S., M. Widmann, V. P. Dymnikov, J. M. Wallace, and I. Bladé (1999), The effective number of spatial degrees of freedom of a time-varying field, *J. Clim.*, *12*(7), 1990–2009.

Chereskin, T. K., and M. Trunnell (1996), Correlation scales, objective mapping, and absolute geostrophic flow in the California current, *J. Geophys. Res.*, *101*(C10), 22,619–22,629.

Cohen, L. (1992), Convolution, filtering, linear systems, the Wiener-Khinchin theorem: Generalizations, *Int. Soc. Opt. Eng.*, *1770*, 378–393, doi:10.1117/12.130944.

Cohen, L. (1998), Generalization of the Wiener-Khinchin theorem, *IEEE Signal Process. Lett.*, *5*(11), 292–294.

Denman, K. L., and H. J. Freeland (1985), Correlation scales, objective mapping and a statistical test of geostrophy over the continental shelf, *J. Mar. Res.*, *43*, 517–539.

de Paolo, T., and E. J. Terrill (2007), Properties of HF radar compact antenna arrays and their effect on the MUSIC algorithm, in *Oceans 2007: Vancouver, BC, Canada, 29 September–4 October, 2007*, pp. 1–10, doi:10.1109/OCEANS.2007.4449265, Inst. of Electr. and Electr. Eng., Piscataway, N. J.

Ekman, V. W. (1905), On the influence of the Earth's rotation on ocean-currents, *Ark. Mat. Astron. Fys.*, *2*, 1–53.

Erofeeva, S. Y., G. D. Egbert, and P. M. Kosro (2003), Tidal currents on the central Oregon shelf: Models, data, and assimilation, *J. Geophys. Res.*, *108*(C5), 3148, doi:10.1029/2002JC001615.

Essen, H.-H., K.-W. Gurgel, and F. Schirmer (1983), Tidal and wind-driven parts of surface currents, as measured by radar, *Dtsch. Hydrogr. Z.*, *36*(3), 81–96.

Ewing, G. C. (1950), Relation between band slicks at the surface and internal waves in the sea, *Science*, *111*(2874), 91–94.

Gonella, J. (1972), A rotary-component method for analysis in meteorological and oceanographic vector time series, *Deep Sea Res. Oceanogr. Abstr.*, *19*, 833–846.

Gough, M. K., N. Garfield, and E. McPhee-Shaw (2010), An analysis of HF-radar measured surface currents to determine tidal, wind-forced and seasonal circulation in the Gulf of the Farallones, California (USA), *J. Geophys. Res.*, *115*, C04019, doi:10.1029/2009JC005644.

Inman, J. R. (1975), Resistivity inversion with ridge regression, *Geophysics*, *40*(5), 798–817.

Kaplan, D. M., J. Largier, and L. W. Botsford (2005), HF radar observations of surface circulation off Bodega Bay (northern California, USA), *J. Geophys. Res.*, *110*, C10020, doi:10.1029/2005JC002959.

Kim, S. Y. (2009), Coastal ocean studies in southern San Diego using high-frequency radar derived surface currents, Ph.D. thesis, Scripps Inst. of Oceanogr., Univ. of Calif. San Diego, La Jolla, Calif. (Available at http://escholarship.org/uc/item/2z5660f4.)

Kim, S. Y. (2010), Observations of submesoscale eddies using high-frequency radar-derived kinematic and dynamic quantities, *Cont. Shelf Res.*, *30*, 1639–1655, doi:10.1016/j.csr.2010.06.011.

Kim, S. Y., E. J. Terrill, and B. D. Cornuelle (2007), Objectively mapping HF radar-derived surface current data using measured and idealized data covariance matrices, *J. Geophys. Res.*, *112*, C06021, doi:10.1029/2006JC003756.

Kim, S. Y., E. J. Terrill, and B. D. Cornuelle (2008), Mapping surface currents from HF radar radial velocity measurements using optimal interpolation, *J. Geophys. Res.*, *113*, C10023, doi:10.1029/2007JC004244.

Kim, S. Y., B. D. Cornuelle, and E. J. Terrill (2009a), Anisotropic response of surface currents to the wind in a coastal region, *J. Phys. Oceanogr.*, *39*, 1512–1533, doi:10.1175/2009JPO4013.1.

Kim, S. Y., E. J. Terrill, and B. D. Cornuelle (2009b), Assessing coastal plumes in a region of multiple discharges: The U.S.–Mexico border, *Environ. Sci. Technol.*, *43*(19), 7450–7457, doi:10.1021/es900775p.

Kim, S. Y., B. D. Cornuelle, and E. J. Terrill (2010), Decomposing observations of high-frequency radar-derived surface currents by their forcing mechanisms: Locally wind-driven surface currents, *J. Geophys. Res.*, doi:10.1029/2010JC006223, in press.

Kirwan, A. D., G. McNally, S. Pazan, and R. Wert (1979), Analysis of surface current response to wind, *J. Phys. Oceanogr.*, *9*, 401–412.

Large, W. G., and S. Pond (1981), Open ocean momentum flux measurements in moderate to strong winds, *J. Phys. Oceanogr.*, *11*, 324–336.

Lumpkin, R. (1995), Resonant coastal waves and superinertial oscillations, Ph.D. thesis, Univ. of Hawaii at Mānoa, Honolulu.

Mooers, C. N. K. (1973), A technique for the cross spectrum analysis of pairs of complex-valued time series, with emphasis on properties of polarized components and rotational invariants, *Deep Sea Res. Oceanogr. Abstr.*, *20*, 1129–1141.

Munk, W. H., and D. E. Cartwright (1966), Tidal spectroscopy and prediction, *Philos. Trans. R. Soc. London A*, *259*(1105), 533–581.

Munk, W. H., B. Zetler, and G. W. Groves (1965), Tidal cusps, *Geophys. J.*, *10*, 211–219.

Ng, B. (1993), The prediction of nearshore wind-induced surface currents from wind velocities measured at nearby land stations, *J. Phys. Oceanogr.*, *23*, 1609–1617.

Paduan, J. D., and M. S. Cook (1997), Mapping surface currents in Monterey Bay with CODAR-type HF radar, *Oceanography*, *10*, 49–52.

Paduan, J. D., and I. Shulman (2004), HF radar data assimiltion in the Monterey Bay area, *J. Geophys. Res.*, *109*, C07S09, doi:10.1029/2003JC001949.

Pawlowicz, R., B. Beardsley, and S. Lentz (2002), Classic tidal harmonic analysis including error estimates in MATLAB using T_TIDE, *Comput. Geosci.*, *28*, 929–937.

Peters, H., L. K. Shay, A. J. Mariano, and T. M. Cook (2002), Current variability on a narrow shelf with large ambient vorticity, *J. Geophys. Res.*, *107*(C8), 3087, doi:10.1029/2001JC000813.

Ponte, A. L. (2010), Periodic wind-driven circulation in an elongated and rotating basin, *J. Phys. Oceanogr.*, *40*, 2043–2058, doi:10.1175/2010JPO4235.1.

Ponte, R. M., and S. V. Vinogradov (2007), Effects of stratification on the large scale ocean response to barometric pressure, *J. Phys. Oceanogr.*, *37*, 245–258, doi:10.1175/JPO3010.1.

Prandle, D. (1987), The fine-structure of nearshore tidal and residual circulations revealed by HF radar surface current measurements, *J. Phys. Oceanogr.*, *17*, 231–245.

Prandle, D., and R. Player (1993), Residual currents through the Dover Strait measured by HF radar, *Esturaine Coastal Shelf Sci.*, *37*, 635–653.

Priestley, M. B. (1981), *Spectral Analysis and Time Series*, 890 pp., Academic Press, London.

Ray, R. D., and G. D. Egbert (2004), The global S_1 tide, *J. Phys. Oceanogr.*, *34*, 1922–1935.

Rosenfeld, L., I. Shulman, M. Cook, J. Paduan, and L. Shulman (2009), Methodology for a regional tidal model evaluation, with application to central California, *Deep Sea Res. Part II*, *56*, 199–218, doi:10.1016/j.dsr2.2008.08.007.

Shay, L. K., H. C. Graber, D. B. Ross, and R. D. Chapman (1995), Mesoscale ocean surface current structure detected by high-frequency radar, *J. Atmos. Oceanic Technol.*, *12*, 881–900.

Spargo, E. A., J. J. Westerink, J. Richard A. Luettich, and D. J. Mark (2004), ENPAC 2003: A tidal constituent database for eastern north

Pacific Ocean, *Tech. Rep. ERDC/CHL TR-04-12*, Coastal and Hydraul. Lab., U.S. Army Corps of Eng., Washington, D. C.

Townsend, A. A. (1980), *The Structure of Turbulent Shear Flow*, 2nd ed., 444 pp., Cambridge Univ. Press, Cambridge, U. K.

von Storch, H., and F. Zwiers (1999), *Statistical Analysis in Climate Research*, 484 pp., Cambridge Univ. Press, Cambridge, U. K.

Wilkin, J. L., M. M. Bowen, and W. J. Emery (2002), Mapping mesoscale currents by optimal interpolation of satellite radiometer and altimeter data, *Ocean Dyn.*, *52*, 95–103, doi:10.1007/s10236-001-0011-2.

Willis, J. K., and L.-L. Fu (2008), Combining altimeter and subsurface float data to estimate the time-averaged circulation in the upper ocean, *J. Geophys. Res.*, *113*, C12017, doi:10.1029/2007JC004690.

Winant, C. D., and A. W. Bratkovich (1981), Temperature and currents on the southern California shelf: A description of the variability, *J. Phys. Oceanogr.*, *11*, 71–86.

Wunsch, C. (1996), *The Ocean Circulation Inverse Problem*, 442 pp., Cambridge Univ. Press, Cambridge, U. K.

Zaron, E., C. Chavanne, G. Egbert, and P. Flament (2009), Baroclinic tidal generation in the Kauai Channel inferred from high-frequency radar doppler currents, *Dyn. Atmos. Oceans*, *48*, 93–120, doi:10.1016/j.dynatmoce.2009.03.002.

B. D. Cornuelle, Climate, Atmospheric Science and Physical Oceanography, Scripps Institution of Oceanography, University of California, San Diego, 9500 Gilman Dr., La Jolla, CA 92093, USA.

S. Y. Kim and E. J. Terrill, Marine Physical Laboratory, Scripps Institution of Oceanography, University of California, San Diego, 9500 Gilman Dr., La Jolla, CA 92093, USA. (syongkim@mpl.ucsd.edu)